Investigation of the Paschen curve for helium in the 100–1000 kV range

Cite as: Phys. Plasmas **24**, 093511 (2017); https://doi.org/10.1063/1.5000387
Submitted: 01 May 2017 . Accepted: 15 August 2017 . Published Online: 01 September 2017

Liang Xu, Alexander V. Khrabrov, Igor D. Kaganovich, and Timothy J. Sommerer

Investigation of the Paschen curve for helium in the 100–1000 kV range

Liang Xu,[1,2] Alexander V. Khrabrov,[2] Igor D. Kaganovich,[2] and Timothy J. Sommerer[3]
[1]*CAS Key Laboratory of Geospace Environment, Department of Modern Physics, University of Science and Technology of China, Hefei, Anhui 230026, China*
[2]*Princeton Plasma Physics Laboratory, Princeton, New Jersey 08543, USA*
[3]*General Electric Global Research, Niskayuna, New York 12309, USA*

(Received 1 May 2017; accepted 15 August 2017; published online 1 September 2017)

The left branch of the Paschen curve for helium gas is studied both experimentally and by means of particle-in-cell/Monte Carlo collision (PIC/MCC) simulations. The physical model incorporates electron, ion, and fast atom species whose energy-dependent anisotropic scattering on background neutrals, as well as backscattering at the electrodes, is properly accounted for. For the range of breakdown voltage $15\,\text{kV} \leq V_{\text{br}} \leq 130\,\text{kV}$, a good agreement is observed between simulations and available experimental results for the discharge gap $d = 1.4\,\text{cm}$. The PIC/MCC model is used to predict the Paschen curve at higher voltages up to 1 MV, based on the availability of input atomic data. We find that the pd similarity scaling does hold and that above 300 kV, the value of pd at breakdown begins to increase with increasing voltage. To achieve good agreement between PIC/MCC predictions and experimental data for the Paschen curve, it is essential to account for impact ionization by fast atoms (produced in charge exchange) and ions and for anisotropic scattering of all species on background atoms. With the increase of the applied voltage, energetic fast atoms progressively dominate in the overall ionization rate. The model makes this clear by predicting that breakdown would occur even without electron- and ion-induced ionization of the background gas, due to ionization by fast atoms backscattered at the cathode, and their high production rate in charge exchange collisions. Multiple fast neutrals per ion are produced when the free path is small compared to the electrode gap. *Published by AIP Publishing.*
[http://dx.doi.org/10.1063/1.5000387]

I. INTRODUCTION

High voltage holding by gas-filled gaps at low pressure, that is, avoiding ionization breakdown, is of interest in important applications, such as high-power switches for electrical power transmission and particle accelerators. Therefore, there is a need to map the Paschen curve, which gives the breakdown voltage V_{br} as a function of the reduced gas pressure pd, where p is the gas pressure and d is the separation between parallel-plate electrodes. The Paschen curve $V = V_{\text{br}}(pd)$ reaches a minimum at some value of pd, which separates the left (low pressure) and the right (high pressure) branches. It is the left branch of the curve that is of interest here.

The breakdown properties of gases, especially noble gases, had been studied by various methods since the early years of research into gas discharge physics.[1–11] For helium gas, the subject of this work, accurate and consistent results exist for applied voltage up to about 1 kV on the low-pressure branch of the Paschen curve. For the range of $10^3 - 10^4$ V, the Paschen curves obtained both by analytical calculation[12] and through particle simulations[13] are not in good agreement with experimental results, for reasons not yet fully understood. There is not a large body of work for higher applied voltage in the range of 100 kV and above, for helium or other gases, but the fundamental approach to the theory and simulations has been developed.[14–17] Specific references to the previous work will be made in what follows.

For parallel-plate DC discharge, the Townsend equation[1] is known to define the breakdown condition near the Paschen minimum and on the high-pressure branch

$$\gamma(e^{\alpha d} - 1) = 1, \tag{1}$$

where α and γ are known as the first and second Townsend coefficients.[18] The underlying assumption of the Townsend theory is that electrons attain a local equilibrium, that is, the electron velocity distribution function (EVDF) is controlled by the local value of the electric field. At the same time, it has been known[2,19–21] that non-equilibrium phenomena resulting in dependence of the EVDF upon the spatial profile of the applied potential take place under conditions corresponding to the left branch of the Paschen curve. Another non-local process involving electrons is ionization by the trapped population backscattered at the anode (the δ-process). Experimental evidence of it was seen in the observed dependence of the breakdown point on the anode material.[22] Other authors[12,14–17,23,24] have established an additional important role of heavy species, namely, ion-impact ionization and fast-atom induced secondary electron emission (as well as the role of non-local ionization by electrons backscattered at the anode, although these early works did not account for backscattering of ions and fast neutrals at the cathode). For helium, in particular, these processes were found to take effect at $pd \sim 1.5\,\text{Torr cm}$ and $V_{\text{br}} \sim 1\,\text{kV}$.[13] Gas ionization by impact of fast neutral atoms produced in charge exchange was also considered in Refs. 14, 15, and 17, in application to

high-voltage discharge in D_2. The work[25] demonstrated the role of gas ionization by fast atoms at $E/n > 15\,\mathrm{kTd}$ ($1\,\mathrm{kTd} = 10^{-18}\,\mathrm{Vm}^2$) in the case of argon. Thus, at sufficiently high values of the reduced electric field E/n, Eq. (1) is no longer adequate to define the breakdown condition, due to both the non-equilibrium behavior of electrons and to the importance of impact ionization by ions and fast atoms.

Furthermore, the heavy species themselves also exhibit non-equilibrium behavior. For example, measurements of ion energy distributions at the cathode of low-current, uniform-field discharges by Rao *et al.*[26] indicate that local-field equilibrium fails to predict the flux-energy distribution for Ar^+ and Ne^+ ions when $E/n > 20\,\mathrm{kTd}$, and for He^+ when $E/n > 10\,\mathrm{kTd}$. Lawler[27] has shown that in the cathode fall of a glow discharge in helium, the length required for He^+ velocity distribution to attain its local-equilibrium form is several times the mean free path (when this length is small compared to that of the cathode fall). Then, it follows that one also needs to account for non-equilibrium behavior of fast atoms produced in charge-transfer collisions, as their velocity distribution is governed by that of the ions. Direct kinetic simulation, therefore, is of interest as a modeling tool that can reproduce the non-equilibrium behavior of energetic electrons, ions, and fast atoms and examine the breakdown process under very high voltage and low pressure. This effort was also started in the works[14–17] cited above.

At present, we investigate the direct-current ionization breakdown in helium gas at applied voltage in the range of several hundred kV (below 1 MV) and reduced pressures $pd < 1\,\mathrm{Torr\,cm}$ (corresponding to the low-pressure branch of the Paschen curve), and offer additional insight into the physics of the breakdown process in this regime. A particle-in-cell/Monte Carlo collision (PIC/MCC) model incorporating electrons, ions, and fast neutral atoms has been formulated to properly describe their interactions with the background gas and with the electrode surfaces. Energy-dependent anisotropic scattering of each species on neutral atoms is considered in detail. In addition, the model accounts for backscattering of heavy particles: ions (with neutralization) at the cathode and fast neutrals at both the cathode and the anode. We compare the simulation results with an existing set of experimental data. The specific details of the simulation model are given in Sec. II and the experiment is described in Sec. III. In Sec. IV, we present and discuss the results. The work is summarized in Sec. V.

II. SIMULATION MODEL

In order to simulate the motion of electrons, He^+ ions, and fast He^0 atoms in a parallel-plate device, we employ the well validated 1D3V code EDIPIC (Electrostatic Direct Implicit Particle-in-Cell).[28] This code has been applied to a number of problems in non-local kinetics and gas discharges, e.g., Refs. 29 and 30. A fast-neutral-atom species that can undergo elastic, excitation, and ionization collisions with the background gas has been added to the numerical scheme. The fast atoms originate primarily in charge-exchange collisions between ions and ambient gas atoms at energies above $\sim$100 eV. In the code, fast atoms are tracked until their kinetic energy falls below twice the ionization potential, to exclude atoms that are not capable of inducing ionization. A fast atom or ion reaching the cathode surface can be backscattered (always as a neutral atom) with an energy-dependent probability. Likewise, additional backscattering can take place at the anode. We note, before referring to the specific details, that the model captures an important self-organization mechanism of sustaining a discharge current in a very high electric field where a beam of backscattered fast atoms ionizes gas atoms in the gap, and the resulting ions undergo multiple cycles of acceleration and charge-exchange collisions to regenerate the primary fast atoms beam that impinges upon the cathode.

The main input parameters to the model are the applied anode voltage, V (the cathode is grounded), the gap width, d, the neutral gas density, n, and the initial plasma density, n_0. In our simulations $n_0 = 1.0 \times 10^{11}\,\mathrm{m}^{-3}$, a somewhat arbitrary low value corresponding to the creation of electron-ion pairs by background cosmic radiation. The Poisson solver remains active in the simulation code, but the plasma density is always small enough to avoid nonlinearity in the eventual steady state due to space charge formation. As long as such is the case, the breakdown condition is not sensitive to the value of n_0. The electrode spacing $d = 1.4\,\mathrm{cm}$ is that of the experimental device described in Sec. III (with a note that the Paschen scaling law still applies, as stated in Sec. IV). The cell size $\Delta x = 20\,\mu\mathrm{m}$ (700 cells within the electrode gap) is sufficient to resolve the smallest scale, defined in the present case by the charge-exchange free path. The most restrictive time-resolution requirement for the problem at hand is that the collision probability for rapidly accelerating electrons in a high electric field undergoes a small relative change over a single simulation step. The value $\Delta t = 0.1\,\mathrm{ps}$ proves sufficient for this purpose. Electrons are at present treated as non-relativistic. Although this is incorrect for energies in the range of several hundred keV, the high-energy electrons are in the runaway regime and their contribution to the ionization rate is small.[21,31] The initial charged-particle population is represented by 500 macro-particles per cell per species, to keep the noise level low. The large number of particles assures reproducibility in numerical breakdown experiments. The material properties of the electrodes correspond to molybdenum at the cathode and to stainless steel (approximated by iron) at the anode, in accordance with the conditions of the experiment. The anode surface is the plane $x = 0$, with spatial uniformity assumed in the $y - z$ plane. The particle dynamics is governed by acceleration in the electric field and by collisions with the background gas, tracked with the Monte Carlo technique. The elementary gas-phase collision processes considered in the model are listed in Table I and their cross-sections are plotted in Fig. 1.

A. Note on input data for neutral-neutral ionization and the role of metastable atoms

An essential ingredient of the breakdown model is a data set of cross-sections $\sigma(\varepsilon)$ for producing an ion-electron pair in neutral-neutral collisions, in this case including both stripping of the fast projectile and ionization of the thermal

TABLE I. Gas-phase elementary physical processes implemented in the model. The corresponding cross-sections are plotted in Fig. 1.

No.	Reaction	Reaction type	Cross-section source
1	$e + \mathrm{He} \rightarrow e + \mathrm{He}$	Elastic collision	32
2	$e + \mathrm{He} \rightarrow e + \mathrm{He}^*$	Excitation collision	33
3	$e + \mathrm{He} \rightarrow 2e + \mathrm{He}^+$	Ionization collision	33
4	$\mathrm{He}^+ + \mathrm{He} \rightarrow \mathrm{He}^+ + \mathrm{He}_{(\mathrm{f})}$	Elastic collision	34
5	$\mathrm{He}^+ + \mathrm{He} \rightarrow \mathrm{He}_\mathrm{f} + \mathrm{He}^+$	Charge exchange collision	35
6	$\mathrm{He}^+ + \mathrm{He} \rightarrow \mathrm{He}^+ + \mathrm{He}^*$	Excitation collision	36
7	$\mathrm{He}^+ + \mathrm{He} \rightarrow 2\mathrm{He}^+ + \mathrm{e}$	Ionization collision	37
8	$\mathrm{He}_\mathrm{f} + \mathrm{He} \rightarrow \mathrm{He}_\mathrm{f} + \mathrm{He}_{(\mathrm{f})}$	Elastic collision	38
9	$\mathrm{He}_\mathrm{f} + \mathrm{He} \rightarrow \mathrm{He}_\mathrm{f} + \mathrm{He}^*$	Excitation collision	39
10	$\mathrm{He}_\mathrm{f} + \mathrm{He} \rightarrow \mathrm{He}_\mathrm{f}^{(+)} + \mathrm{He}^{(+)} + e$	Ionization collision	40, 41

The subscript "(f)" indicates a possibility for an atom to be produced as a fast neutral in the respective collision.
He_f denotes fast He atoms capable of impact ionization.

target. The collision energy of interest for breakdown calculations is $\varepsilon \approx 0.1\,V_{\mathrm{br}}$, because the electrode separation distance is about 10 times the mean-free path for charge exchange λ_{cx} at conditions corresponding to the left branch of the Paschen curve. Data from various experimental[40,42–45] and theoretical[46,47] estimates of cross-sections for helium are in reasonable agreement near their maximum value, around 150 keV, where the impact velocity is comparable to that of the upper-shell electron in an atom, but increasing discrepancies occur at low projectile energies (below 20 keV, corresponding to 10 keV in the center-of-mass frame), where the cross-sections are relatively small. Some of the available experimental data for helium neutral/neutral ionization cross-sections are plotted in Fig. 2, where the discrepancies in the low-energy range are clearly seen. In the low-energy range, we choose the data of Hayden and Utterback,[40] because it is the one most commonly used in numerical

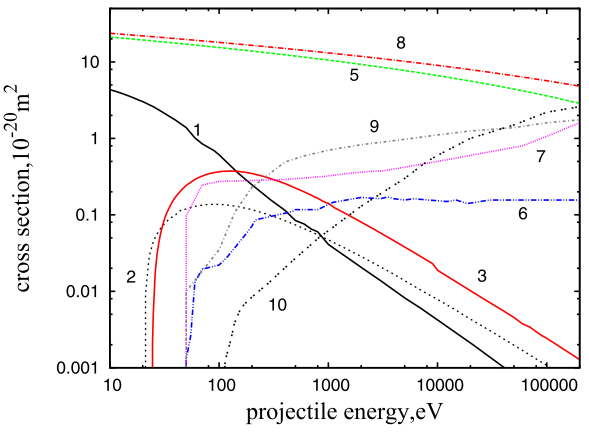

FIG. 1. Cross-sections for (1) elastic scattering of electrons, (2) electron-impact excitation, (3) electron-impact ionization, (5) ion-atom symmetric charge exchange, (6) ion-impact excitation, (7) ion-impact ionization, (8) elastic scattering of atoms, (9) atom-impact excitation, and (10) atom-impact ionization. The cross-section for ion-atom elastic collision, process (4), can be neglected for the purpose of this study in comparison to the cross-section of ion-atom charge exchange. Cross-section of the process (6) in the range between 20 keV and 200 keV is extrapolated from the data below 20 keV in Ref. 36.

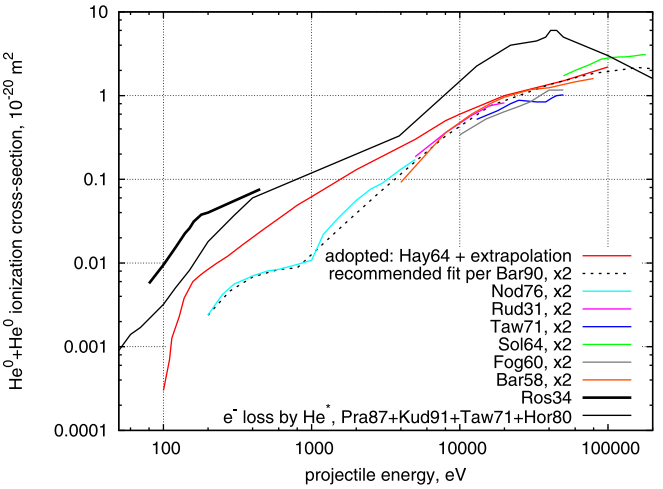

FIG. 2. Cross-sections for neutral-neutral impact ionization in helium gas. The discrepancies between data from available sources prevail at lower energies. Cross-sections for electron loss by metastable atoms (beam of mostly triplets) are also shown. The cited sources are as follows: Hay64,[40] Bar90,[41] Nod76,[45] Rud31,[42] Taw71,[57] Sol64,[58] Fog60,[59] Bar58,[60] Ros34,[43] Pra87,[61] Kud91,[62] Hor80.[53] The data in Bar90 are a fit to several combined experimental data sets above 4 keV, and to Ref. 45 below 4 keV. Cross-sections obtained for the stripping process only (electron loss by fast atoms) in symmetric collisions were multiplied by 2. Much of the above data are tabulated in the review[63] and atomic collision database.[64]

simulations of discharges in helium, and as will be shown in Sec. IV A, because satisfactory agreement is obtained between the theoretical and experimental Paschen curves.

The measurements of Hayden and Utterback[40] are available for $\varepsilon < 1$ keV. Smooth interpolation was adopted for higher energies as shown in Fig. 2. We note that in the range of 100 eV $< \varepsilon <$ 600 eV, the cross-sections reported in Ref. 40 agree with those of Hammond *et al.*[44] (not shown), although the latter authors relied on the former for absolute calibration of the results. At the same time, the plots in Fig. 2 indicate that the measurements of Noda,[45] available for ε up to 5 keV, smoothly join to the values obtained by others at higher energies.

One may attempt to resolve the discrepancies at low energy by accounting for the presence of a fraction of metastable atoms in the neutral helium beams that are formed in experimental work. Metastable He atoms, with ionization energy under 5 eV, have much higher electron-loss cross-sections than ground-sate atoms. The respective experimental cross-sections are also presented in Fig. 2. However, this explanation does not apply at low energies, where the cross-sections for production of metastable atoms during charge exchange collisions are quite small,[48–50] about 1% of the full cross-section of charge exchange. On the other hand, the cross-section of the resonant de-excitation process scales similarly to charge exchange.[51–53] At energies below 10 keV, it is on the order of 10^{-15} cm^2. Lastly, the metastable fraction in the neutral beam may vary between different experiments (depending, e.g., on the length of the neutralizer cell) and the only way to properly account for the effect of metastable atoms is to include their kinetics (including surface interactions) in the physical model. This improvement should be one of the directions for future work on the subject.

For helium, similar uncertainty exists with respect to cross-section data for atom ionization by energetic ion impact. For example, two sets of data on free-electron-production cross-section,[54,55] which were obtained by the same group, strongly diverge for energies below 100 keV. Theoretically derived values[56] agree with the smaller ones of Ref. 55 within the experimental range, and fall off sharply to below 10^{-18} cm^2 at $\varepsilon = 10$ keV. These cross-sections, however, are not as critical for modeling high-voltage breakdown as those of neutral-impact ionization, because ions are re-accelerated after each collision and produce multiple fast neutral atoms via charge exchange.

B. Time-advance and the breakdown criterion

In the Monte Carlo collision model, a particle with energy ε moving through a set of scatterers with density n can undergo a collision (of any type among those allowed) over a simulation time step Δt with a probability

$$P = 1 - \exp\left[-\Delta t \nu(\varepsilon)\right] \approx \Delta t \nu(\varepsilon), \tag{2}$$

where $\nu(\varepsilon) = v\sigma_{\rm sc}(\varepsilon)n$ is the collision frequency, $\sigma_{sc}(\varepsilon)$ is the energy-dependent total cross-section for the respective species, $v = (2\varepsilon/m)^{1/2}$ is the particle velocity, and m is the particle mass. The type of elementary collision to occur within the time step is selected, as usual, by the rejection method based on cumulative probability values.[28] For fast atoms, the energy remains constant during the free flight. Recently, the simulation code has been comprehensively validated by reproducing experimental measurements in a glow discharge.[30]

The DC breakdown, of interest in this work, occurs when the gas ionization rate due to the applied electric field is sufficient to create a self-sustained electric current. The breakdown threshold is defined as the condition where a steady state is attained, with a local balance between ionization and fluxes of ions and electrons. The production rate of ion-electron pairs due to impact ionization in the volume should equal the net ion flux $\Gamma_{\rm i,net}$ (or net electron flux $\Gamma_{\rm e,net}$) calculated at the boundaries

$$\Gamma_{\rm e,net}(x) = \Gamma_{\rm i,net}(x) = \int_0^x \left[Z_{\rm ei}(x') + Z_{\rm ii}(x') + Z_{\rm ai}(x')\right] dx', \tag{3}$$

where $Z_{\rm ei}(x)$, $Z_{\rm ii}(x)$, and $Z_{\rm ai}(x)$ are the local ionization rates (production of ion-electron pairs per unit volume per unit time) due to electrons, ions, and fast atoms, and the net flux for both electrons and ions is $\Gamma_{\rm net}(x) = \Gamma(x) - \Gamma(0)$. Figure 3(a) shows an example of a simulation run in which Eq. (3) is satisfied for ions and hence for electrons (the anode flux $\Gamma(0)$ is neglected for the ions). In the model, the anode is set at $x = 0$. In this case, the applied voltage is 100 kV and $n = 1.018 \times 10^{22}$m^{-3}. The elapsed simulation time is 380 ns. Figure 3(b) illustrates the temporal evolution prior to achieving the steady state: the ion densities at the center of the gap, $x = 0.7$ cm and near the cathode, at $x = 1.2$ cm, remain unchanged after an initial transient spike. In what follows, we address the detailed treatment of particle collisions and surface interactions (boundary conditions for particles) in our model.

C. Anisotropic electron scattering on helium atoms

The model for elastic scattering of electrons is designed to reproduce the correct values of both the total, $\sigma_{\rm tot}$, and the momentum-transfer, $\sigma_{\rm mt}$, cross-sections. It utilizes an approximation of energy-dependent screened-Coulomb scattering.[65,66] The normalized differential cross-section writes as

$$\frac{1}{\sigma_{\rm tot}}\frac{{\rm d}\sigma}{d\Omega} = \frac{1}{4\pi}\frac{1-\xi^2(\varepsilon)}{\left[1-\xi(\varepsilon)\cos^2\theta\right]}, \tag{4}$$

where $\sigma_{\rm tot}$ is the total cross-section and θ is the scattering angle. The dimensionless screening function $\xi(\varepsilon)$ is approximated by fitting the value of $\sigma_{\rm mt}(\varepsilon)/\sigma_{\rm tot}(\varepsilon)$ resulting from Eq. (4) with the one based on experimental and/or theoretical cross-section data. For helium, the following approximation was given in[67]

$$\xi(\varepsilon) = 1 + \frac{p_1\sqrt{\varepsilon} - p_2^2 - p_3}{\left(\sqrt{\varepsilon} - p_2\right)^2 + p_3} - \frac{p_1\sqrt{\varepsilon}}{\left(\sqrt{\varepsilon} - p_4\right)^2 + p_5}, \tag{5}$$

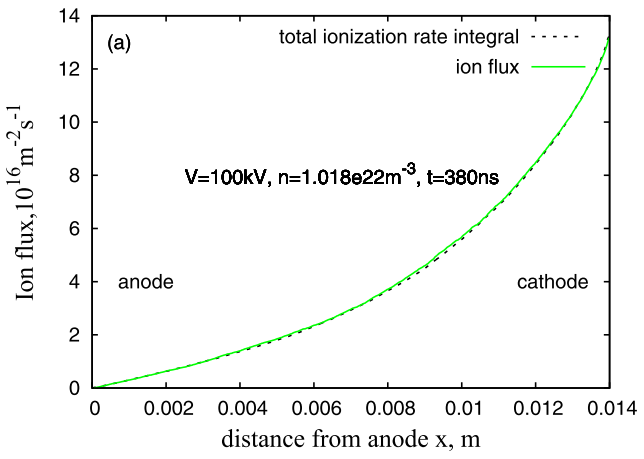

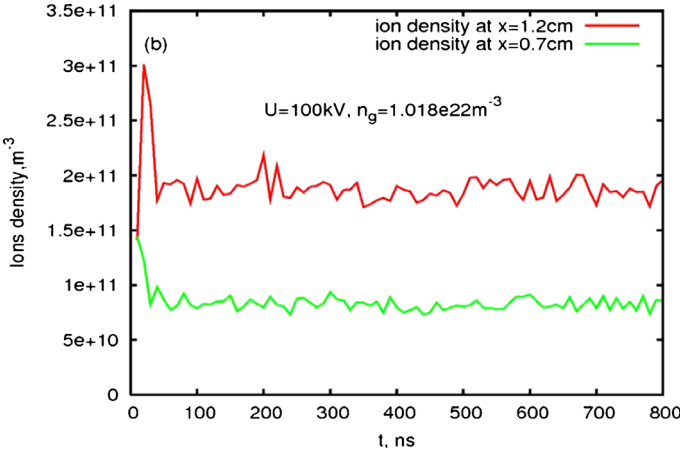

FIG. 3. The criterion for breakdown is that the production of electron-ion pairs by ionization in the gas is equal to the net flux of ions and electrons counted at the electrodes: (a) Running integral of total ionization rate equals the local ion net flux in the gap; the applied voltage is $V = 100$ kV, the gas density is $n = 1.018 \times 10^{22}$m^{-3}, and the elapsed time $t = 380$ ns. (b) Steady state of ion density profile is achieved.

where $p_1 = 2.45, p_2 = 2.82, p_3 = 11.98, p_4 = 5.11, p_5 = 64.01$. The scattering angle θ is sampled by inverting the corresponding cumulative probability as

$$\cos\theta = 1 - \frac{2R[1-\xi(\varepsilon)]}{1+\xi(\varepsilon)(1-2R)}, \tag{6}$$

with the random number R sampled from a uniform distribution on [0,1].

In a standard fashion, the post-collision velocity vector of an electron scattered through a polar angle θ and an azimuthal angle φ can be expressed as follows:

$$u_{sc,x} = u_{inc,x}\cos\theta + \frac{u_{inc,y}u}{\sqrt{u_{inc,x}^2+u_{inc,y}^2}}\sin\theta\sin\varphi + \frac{u_{inc,x}u_{inc,z}}{\sqrt{u_{inc,x}^2+u_{inc,y}^2}}\sin\theta\cos\varphi, \tag{7}$$

$$u_{sc,y} = u_{inc,y}\cos\theta - \frac{u_{inc,x}u}{\sqrt{u_{inc,x}^2+u_{inc,y}^2}}\sin\theta\sin\varphi + \frac{u_{inc,y}u_{inc,z}}{\sqrt{u_{inc,x}^2+u_{inc,y}^2}}\sin\theta\cos\varphi, \tag{8}$$

$$u_{sc,z} = u_{inc,z}\cos\theta - \sqrt{u_{inc,x}^2+u_{inc,y}^2}\sin\theta\cos\varphi, \tag{9}$$

where $u_{sc,x}$, $u_{sc,y}$, and $u_{sc,z}$ are the components of the electron velocity vector after scattering; $u_{inc,x}$, $u_{inc,y}$, and $u_{inc,z}$ are components before scattering, and $u^2 = u_{inc,x}^2 + u_{inc,y}^2 + u_{inc,z}^2$. The code accounts for the small energy loss due to recoil, although this is not essential for the problem at hand.

The scattering procedure defined by Eqs. (4) and (6) is also applied to inelastic collisions, with account for the energy loss. This is done for numerical simplicity and has been known to work well in our verification studies.[30]

The electron-impact excitation of helium atoms is treated as a single-channel process, with the cross-section being a weighted sum over seven closely located levels to yield a correct mean energy loss. When a background atom is excited, the electron energy change is set to be $\Delta\varepsilon = -\varepsilon_{\text{exc}}$, where ε_{exc} is the energy of the lowest excited level. To account for this energy loss, the post-collision velocity components in Eqs. (7)–(9) are multiplied by the factor $\kappa = \sqrt{(\varepsilon+\Delta\varepsilon)/\varepsilon}$. The scattering angle is again sampled by means of Eq. (6) in which the incoming energy ε is replaced with $\varepsilon + \Delta\varepsilon$.

For the electron-impact ionization process, according to Refs. 68 and 69, the energy partition between the ejected (ε_1) and the scattered (ε_2) electrons is approximated as

$$\varepsilon_1 = \omega\tan\left[R\arctan\left(\frac{\varepsilon-\varepsilon_i}{2\omega}\right)\right], \tag{10}$$

$$\varepsilon_2 = \varepsilon - \varepsilon_i - \varepsilon_1, \tag{11}$$

where $\varepsilon_i = 24.6\,\text{eV}$ is the ionization potential of helium and $\omega = 15.8\,\text{eV}$ is also a parameter specific to the gas.[68] The velocity directions of both scattered and ejected electrons are again obtained according to Eq. (6), with the argument ε taking the values ε_1 and ε_2, respectively. Then, the velocity components of both electrons are calculated by applying Eqs. (7)–(9) and multiplying their magnitude with the factors $\kappa_1 = \sqrt{\varepsilon_1/\varepsilon}$ and $\kappa_2 = \sqrt{\varepsilon_2/\varepsilon}$.

D. Anisotropic scattering of helium ions on helium atoms

For the combined process of charge exchange and elastic ion/atom scattering in helium, Wang *et al.*[70] proposed the following numerically treatable approximation for the differential cross-section:

$$\frac{d\sigma}{d\Omega}(\varepsilon,\theta) = \frac{A}{[1-\cos\theta+a(\varepsilon)]^{1.25}} + \frac{A}{[1+\cos\theta+b(\varepsilon)]^{1.25}}, \tag{12}$$

where A, a, and b are fitting parameters chosen to reproduce the correct values of both the momentum transfer cross-section and the viscosity (energy transfer) cross-section of the process. Refer to Ref. 70 for how these values are obtained. Note that the energy in Eq. (12) is the total energy of two colliding particles, the ion and the atom, in their center-of-mass frame of reference. The differential cross-sections for the charge-exchange and for the elastic collision in this case are identified as

$$\frac{d\sigma_{\text{cx}}}{d\Omega}(\varepsilon,\theta) = \frac{A}{[1+\cos\theta+b(\varepsilon)]^{1.25}}, \tag{13}$$

$$\frac{d\sigma_{\text{elast}}}{d\Omega}(\varepsilon,\theta) = \frac{A}{[1-\cos\theta+a(\varepsilon)]^{1.25}}. \tag{14}$$

In the Monte-Carlo procedure, we then formally treat the two processes as independent, i.e., only one kind can occur over a given time step. Based on the differential cross-sections, the scattering angle θ can be calculated from the cumulative probability distribution, just like for the electron-atom collisions. For the elastic collision

$$\cos\theta = 1 + a - \left\{a^{-0.25} - R\left[a^{-0.25} - (2+a)^{-0.25}\right]\right\}^{-4}, \tag{15}$$

and for the charge exchange collision

$$\cos\theta = -1 - b - \left\{(2+b)^{-0.25} + R\left[b^{-0.25} - (2+b)^{-0.25}\right]\right\}^{-4}, \tag{16}$$

where R is a number sampled from a uniform distribution on [0,1]. To calculate the post-collision velocity of the ion, we apply Eqs. (7)–(9) in the center-of-mass frame, before transforming to the laboratory frame.

For the ion-impact excitation process, only a single energy level is considered, as the available data do not allow to fully distinguish between possible channels. The scattering is performed based on Eq. (15) for ion-atom elastic collision. The energy loss $\Delta\varepsilon = -\varepsilon_{\text{exc}}/2$ is taken into account to calculate the scattered velocity in the center-of-mass frame.

Equations (7)–(9) are applied and the rotated velocity vector is rescaled by the factor of $\kappa = \sqrt{(\varepsilon + \Delta\varepsilon)/\varepsilon}$.

For the ion-impact ionization process, we assume simply that the ejected electron has zero energy in the laboratory frame, which is appropriate for high electric fields of interest in the present work. The post-collision velocity components of a scattered ion in the center-of-mass frame are calculated through Eqs. (7)–(9), with multiplying by the factor $\kappa = \sqrt{(\varepsilon - \varepsilon_i/2)/\varepsilon}$, where ε_i is the ionization potential. Finally, the velocity vectors of the scattered and ejected ions are transformed to the laboratory frame. In the center-of-mass frame, we apply the same angular distribution as for the ion-atom elastic collision, substituting $a(\varepsilon - \varepsilon_i/2)$ for $a(\varepsilon)$ in Eq. (15).

E. Anisotropic scattering of fast helium atoms

For the elastic scattering of fast atoms on background thermal neutrals, we can still apply the normalized differential cross-section of the type defined by Eq. (4), but this time, for identical species, aiming to approximate the known ratio of the viscosity cross-section σ_{visc} to the total cross-section σ_{tot}. From Eq. (4), it follows that

$$\frac{\sigma_{\text{visc}}}{\sigma_{\text{tot}}} = 1 - \frac{\left[1-\chi^2(\varepsilon)\right]}{2\chi^3(\varepsilon)} \frac{\chi(\varepsilon)\left[2-\chi^2(\varepsilon)\right]}{1-\chi^2(\varepsilon)} + \ln\left[\frac{1-\chi(\varepsilon)}{1+\chi(\varepsilon)}\right], \tag{17}$$

where the screening function $\chi(\varepsilon)$ is determined by making the above ratio match the one based on the cross-section data (in this case sourced from Ref. 38). A similar approach was employed by Wang *et al.*,[70] cited above, for ion-atom collisions. We obtained the following rational-function approximation for $\chi(\varepsilon)$

$$\chi(\varepsilon) = 1 - \frac{1 + q_4\varepsilon}{q_1 + q_2\varepsilon + q_3\varepsilon^2}, \tag{18}$$

where ε is in eV and $q_1 = 23.022, q_2 = 2.4786, q_3 = 0.00474$, $q_4 = 0.00013$. The scattering angle is sampled according to Eq. (6)

$$\cos\theta = 1 - \frac{2R[1-\chi(\varepsilon)]}{1+\chi(\varepsilon)(1-2R)}. \tag{19}$$

The post-collision velocities of the two neutral atoms are calculated by applying Eqs. (7)–(9) in the center-of-mass frame.

For the fast-atom-impact excitation, only a single energy level 2^1P is assigned to the available cross-section data, similarly to the treatment of ions. The energy loss $\Delta\varepsilon = -\varepsilon_{\text{exc}}/2$ is applied to adjust the post-collision velocity components of both scattered atoms in the center-of-mass frame. After using Eqs. (7)–(9), these vector components are multiplied with a factor $\kappa = \sqrt{(\varepsilon + \Delta\varepsilon)/\varepsilon}$. The scattering angle is chosen using $(\varepsilon + \Delta\varepsilon)$ as an argument of χ in Eq. (19).

For the fast-atom-impact ionization, we impose a symmetry condition for the collision in the center-of-mass frame, since one cannot distinguish which of the atoms is ionized. Thus, the ejected ion originates with equal probability of $1/2$ from the projectile (as identified in the lab frame) or from the target. For the ejected electron, the energy is again assumed to be zero in the laboratory frame. The post-collision velocity of the scattered atom and ion is calculated by applying the factor $\kappa = \sqrt{(\varepsilon - \varepsilon_i/2)/\varepsilon}$, where ε_i is the ionization potential, after using Eqs. (7)–(9). The velocity vectors of the ejected ion and of the scattered atom are opposite in the center-of-mass frame. These velocities are then transformed to the laboratory frame. We apply the same angular distribution as for the elastic collision, now replacing the initial energy ε in Eq. (19) with $(\varepsilon - \varepsilon_i/2)$.

F. Surface interactions

Next, we consider the physical model of energetic particle interactions with electrode surfaces. The interactions to be accounted for are secondary electron emission induced by incident ions and by fast neutral atoms at the cathode, electron backscattering at the anode, backscattering of both ions and fast neutrals at the cathode, and fast neutral backscattering at the anode. For ions and fast neutrals, the typical energy is estimated as $E\lambda_{\text{cx}} = V\lambda_{\text{cx}}/d$ and can be on the order of several tens keV. Electron energies in this regime reach values up to the applied potential.

1. Secondary electron emission

Secondary electrons are emitted from the cathode surface due to impact by ions and by fast atoms, as well as by photons emitted due to excitation of the background gas by electrons, ions, and fast atoms. Each act of excitation is assumed to ultimately yield a photo-emitted electron at the cathode surface, with a probability of 0.15 for a parallel-plate device.[71] Secondary electron yield is one of the crucial inputs of the discharge model and its accuracy greatly influences the outcome. At the same time, there is lack of unambiguous information regarding the properties of the cathode surface exposed to a discharge environment. Previous work[7,24] has shown that the secondary yields measured under ultra-high vacuum conditions, for so-called clean cathode or flashed cathode, are not directly applicable to gas discharge. This is due to the gas layers adsorbed on the surface, other possible contaminants, and sputtering, all of which combine to make what is known as the "dirty" cathode. In our model, the secondary electron yields $\gamma_i(\varepsilon)$ (on a "dirty" molybdenum surface) for ion energies between 1 keV and 20 keV were adopted from Szapiro *et al.*[72] These data were extrapolated to lower and higher energies so that the extrapolated values are in good agreement with the data in the respective ranges as reported in Refs. 40 and 73. Due to the lack of available data for the fast-atom emission yield $\gamma_a(\varepsilon)$ on the molybdenum surface, we assumed the ratio $\gamma_{\text{a}}(\varepsilon)/\gamma_{\text{i}}(\varepsilon)$ to be the same as the ratio of secondary yields for a "clean" cathode, for which experimental data[74] are available. The secondary electron yields are plotted in Fig. 4.

2. Particle reflection at the electrodes

a. Electrons. The model accounts for backscattering of fast electrons at the anode. As noted in the *Introduction*, the importance of this process in the ionization balance was

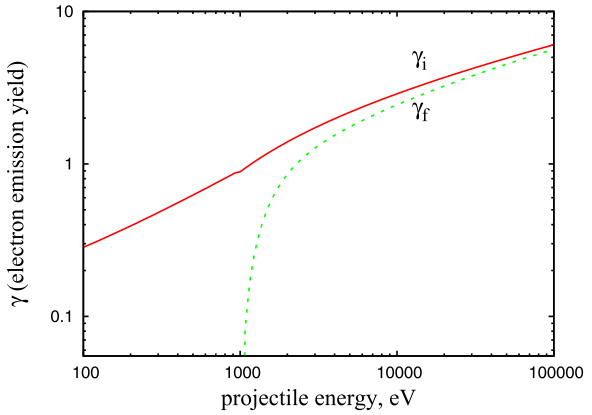

FIG. 4. Adopted secondary electron yields due to ions, γ_i and to fast atoms, γ_f, vs. projectile energy for "dirty" molybdenum surface.

recognized in the early work on models of breakdown at high voltage. More recently, this process was found[13] to be responsible for the multi-valued behavior of the simulated Paschen curve for helium at lower voltage. The probability of backscattering is approximated as a function of the incidence angle only. For a stainless-steel anode, the data available for iron were used to approximate the reflection yield according to Darlington[75] as follows:

$$\eta(\theta) = \eta_0 \exp\left[B(1-\cos\theta)\right], \tag{20}$$

where the values of empirical constants are $\eta_0 = 0.28$ and $B = 1.154$. The angular distribution of the backscattered flux at the surface obeys the cosine law (yielding a half-isotropic distribution in the volume): $\cos\theta = \sqrt{R}$. The energy was sampled according to the approximation $\varepsilon_b = \varepsilon \times R^{0.34}$, based on experimental distributions reported in Ref. 75. As shown above, ε_b is the electron energy after backscattering and R is a random number sampled from a uniform distribution on [0, 1].

b. Atoms and ions. Besides the electron backscattering at the anode, we take into account ion backscattering at the cathode and fast atom backscattering at both electrodes. Note that ions are neutralized when backscattered at the cathode.[76]

The numerical model for backscattering of ions and fast neutrals is based on the work of Eckstein.[77] This comprehensive report provides data on reflection yield as predicted by molecular dynamics for numerous target/projectile combinations. Experimental data are combined with calculations when available. Theoretical particle-flux and energy-flux reflection yield values for normal incidence are represented by analytical fits as functions of the projectile energy. Angular dependencies are also fitted for a tabulated set of energy values. For example, for the molybdenum cathode used in the experimental device, the following fits provide the angular dependence of the flux reflection yield of atoms and ions at $\varepsilon = 8$ keV, and the energy dependence of the yield at normal incidence:

$$\gamma_{\mathrm{n,cathode}}(8\,\mathrm{keV},\theta) = 3.347 + 3.132\tanh \times \left[1.093\pi(\theta/180) - 2.757\right], \tag{21}$$

$$\gamma_{\mathrm{n,cathode}}(\varepsilon,0) = 0.3173(\varepsilon/\varepsilon_0)^{-0.1266}/[1 + 0.2517(\varepsilon/\varepsilon_0)^{1.817}], \tag{22}$$

where $\varepsilon_0 = 9943.65$ eV and the incidence angle is in degrees. The subscript "n" designates the particle, or "number" flux. However, the report[77] also indicates that in the case of molybdenum (as well as zirconium and niobium), experimental values for particle-flux and energy-flux reflection yields can be up to a factor of 3 lower than the theoretically computed predictions in the 10–100 keV projectile energy range of interest to us. Thus, in the PIC/MCC model, we adopted the available experimental data as the input. An analytical fit of the same form as given by Eq. (22) is used to extrapolate the yields to lower and higher projectile energies. The fitted $\gamma_n(\varepsilon,0)$ can be expressed as follows:

$$\gamma_{\mathrm{n,cathode,\,exp}}(\varepsilon,0) = 0.09073(\varepsilon/\varepsilon_0)^{-0.4212}/ [1 + 0.0394(\varepsilon/\varepsilon_0)^2]. \tag{23}$$

The molecular-dynamics prediction (22) of Ref. 77 and our adopted fit (23) to the experimental data cited there are plotted in Fig. 5.

For simplicity, we implemented the particle reflection probability as a function of both energy ε and incident angle, θ (in radians) in the numerical model as follows:

$$\eta_{\mathrm{cathode}}(\varepsilon,0) = \gamma_{n,\mathrm{cathode,expt}}(\varepsilon,0) + \left[1 - \gamma_{n,\mathrm{cathode,expt}}(\varepsilon,0)\right](2\theta/\pi)^3. \tag{24}$$

This form is designed to adequately reproduce numerically predicted angular dependencies which in Ref. 77 were tabulated for a discrete set of incident energies.

The calculated particle-flux reflection coefficient integrated over the energy spectrum and ejection angles of the backscattered atoms must give the energy-flux reflection coefficient, also reported in Ref. 77. The calculated energy-flux reflection yield at normal incidence is approximated by the following fitting function:

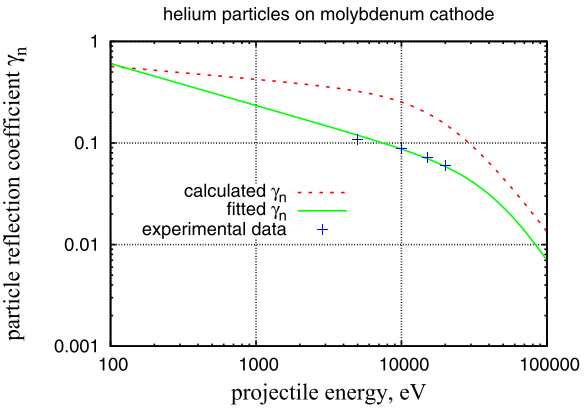

FIG. 5. Fast heavy particle reflection coefficients given by theoretical calculation and by experiment. The green fitted curve is used in our simulations. It is of the same functional form as the red curve from Ref. 77, but the numerical constants have been modified so as to fit the experimental data, also from that work.

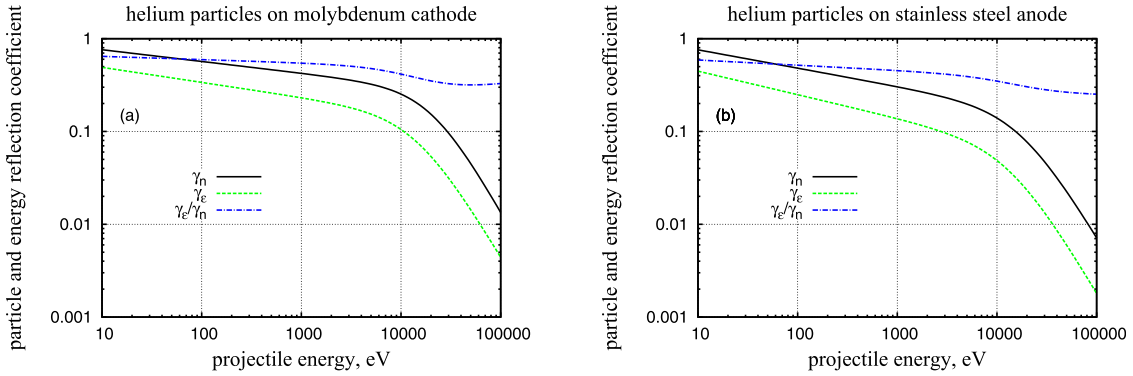

FIG. 6. Fast heavy particle number-flux and energy-flux reflection coefficients and their ratio, which represents the energy change after backscattering (a) for Mo cathode, and (b) for stainless steel anode.

$$\gamma_{\varepsilon,\text{cathode}}(\varepsilon,0) = 0.1607(\varepsilon/\varepsilon_0)^{-0.1616}/[1+0.5242(\varepsilon/\varepsilon_0)^{1.659}]. \tag{25}$$

In principle, this fit also needs to be replaced with a fit to the experimental data. However, only the ratio $\gamma_\varepsilon/\gamma_n$ needs to be known in our model as shown below, and evaluating it from the calculated values of Ref. 77 is accurate enough for our purpose.

Next, for the anode made of stainless steel, the material properties are approximated by those of iron. We assumed the same functional dependence of the particle reflection coefficient on both the incident angle and projectile energy as we did for molybdenum

$$\eta_{\text{anode}}(\varepsilon,0) = \gamma_{\text{n,anode}}(\varepsilon,0) + \left[1-\gamma_{\text{n,anode}}(\varepsilon,0)\right](2\theta/\pi)^3, \tag{26}$$

where $\gamma_{\text{n,}anode}$ is the calculated particle reflection yield for helium atoms (or ions) on iron, at normal incidence[77]

$$\gamma_{\text{n,anode}}(\varepsilon,0) = 0.2179(\varepsilon/\varepsilon_0)^{-0.1976}/[1+0.148(\varepsilon/\varepsilon_0)^{1.621}]. \tag{27}$$

The corresponding energy-flux reflection yield is

$$\gamma_{\varepsilon,\text{anode}}(\varepsilon,0) = 0.09012(\varepsilon/\varepsilon_0)^{-0.2536}/[1+0.2304(\varepsilon/\varepsilon_0)^{1.589}]. \tag{28}$$

In the case of iron, the molecular-dynamics calculations of Ref. 77 are in much better agreement with experimental data than they are for molybdenum.

Due to the lack of data on the energy spectrum of backscattered fast atoms, we adopted the mean energy as the energy of backscattered fast atoms at both electrodes

$$\varepsilon' = \langle \varepsilon_b(\varepsilon,\theta)\rangle = \varepsilon\frac{\gamma_\varepsilon(\varepsilon,0)}{\gamma_n(\varepsilon,0)}, \tag{29}$$

where ε is the energy of the incident ion or atom. To summarize, the particle backscattering of an ion or fast neutral occurs with a probability given by Eq. (24), the energy of the resulting backscattered fast neutral is given by Eq. (29), and the backscattering angle is sampled from a cosine distribution.

Figure 6 presents the numerically predicted particle-flux and energy-flux reflection yields from Ref. 77, along with their ratio, shown for both electrodes.

Self-sputtering is not taken into account because it has little effect near the breakdown point as the current density is very small.

III. EXPERIMENT

Prior to the present work, an experimental study of DC breakdown in helium was conducted with a laboratory device intended to aid in the design of a high-voltage switch. The work will be described in a separate publication, and only a synopsis is given here. The switch is shown in Fig. 7. A similar device (with concentric cylindrical electrodes) was described in Ref. 78, along with its operation as a pulsed-power switch. Here, the discharge gap is between planar electrodes with a separation of 1.4 cm. The anode is made of stainless steel. It is 15 cm in diameter, with edges rounded to 1.5 cm radius to reduce non-uniformity of the electric field. Electrostatic simulations indicate that the field near the electrode surfaces at the intersection between the planar and rounded regions is 14% higher than the field in the planar gap. The anode fits tightly into an alumina insulator, with only 0.5 mm radial separation between the inner surface of the insulator and the anode, so as to prevent long-path gas breakdown in the annulus. The negative electrode for the

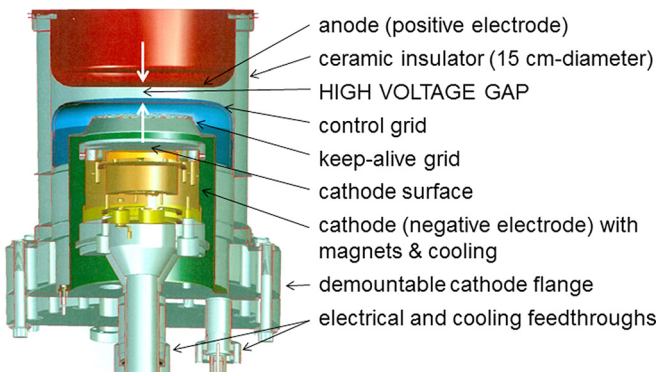

FIG. 7. Experimental setup for studying high-voltage breakdown in helium. The experiments were conducted in a technical device used for high-voltage switching. The high-voltage gap is between the control grid and the anode, as indicated by white arrows.

breakdown measurements is the so-called control grid (CG) of the switch. The control grid is a shell of arc-cast molybdenum, machined from solid stock to a thickness of 0.5 mm. The planar region of the CG is patterned with an array of 1 mm-diameter laser-drilled holes, with center-to-center spacing 1.115 mm, that are necessary to conduct the plasma current when the switch is closed. Like the anode, the cathode edges are rounded to a 1.5 cm radius, and it fits tightly within the alumina insulator (1 mm gap), to avoid long-path breakdown in the annulus. The remaining structures in the switch—the keep-alive grid (KAG) and the actual switch cathode — are electrically connected to the CG for breakdown measurements, and the CG, KAG, and switch cathode are all tied to ground. The cathode contains magnets that are important when the switch is conducting current, but the field strength falls rapidly with distance from the cathode surface, and they do not affect the gas breakdown properties of the high-voltage gap.

The molybdenum CG and the anode were chemically etched to remove asperities. After assembly and vacuum-welding the device was baked at 250 °C under vacuum for 24 h. Vacuum is provided by a turbopump backed with a roughing pump in the form of an integrated pumping station [Pfeiffer Vacuum HiCube Classic Pumping Station], and the pressure is limited during the bake to few mTorr. Hydrogen is the main contaminant seen in the residual gas analyzer. Higher baking temperature was not possible because of braze alloys in the device. A similar vacuum system is used during high-voltage testing, and the base pressure is 10^{-7} Torr.

High-voltage measurements are performed with the anode connected to a high-voltage supply [Spellman Model ST150*10] through a 5 MΩ series resistor. High purity helium gas is admitted to the device through a leak valve to the desired pressure. A single set of data was obtained as follows: at a given pressure p, the anode voltage is raised until a flash of current is observed through a current probe that is connected between the CG and ground and then held constant for 20 min. This value was recorded as the breakdown voltage for given pressure. The results are shown as the data points in Fig. 8.

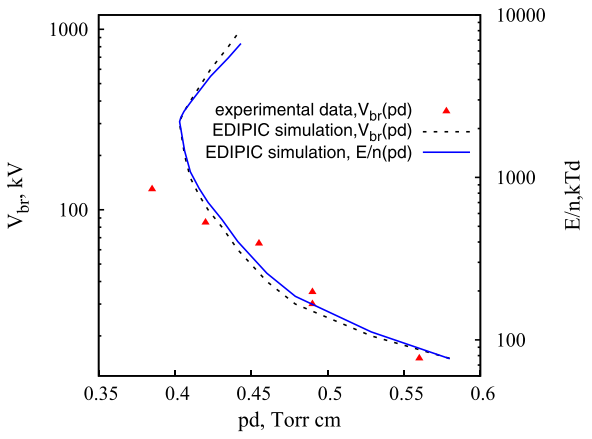

FIG. 8. Paschen curves, parametrized by both voltage $V_{br}(pd)$ and by reduced electric field $\frac{E}{n}(pd)$, derived from PIC/MCC simulations and compared to experimental data.

Initial tests without added gas indicated that the vacuum breakdown threshold was above 150 kV, corresponding to an electric field of 107 kV/cm in the planar gap and 122 kV/cm near the electrode surfaces at the aforementioned transition between the planar and rounded regions. After some experimentation, subsequent tests with gas in the device were conducted with a small gas flow through the leak valve, balanced by the vacuum pump and a throttling valve. The final device seal is a conventional copper gasket and bolted flange, so we expect that impurities accumulate in the gas over time, and that the small gas flow removes them.

IV. RESULTS AND DISCUSSION

In Sec. IV A, we present the Paschen curve resulting from our simulations and compare it with experimental data, and also discuss the breakdown mechanism. The remainder of the section is aimed at providing insight into the physics of the process. First, individual roles of principal elementary interactions are examined: backscattering of fast neutral atoms in Sec. IV B, and gas ionization by atoms and ions in Sec. IV C. The effect of anisotropic scattering of fast atoms is considered in Sec. IV D. Energy-flux distributions of individual species arriving at the electrodes are studied in Sec. IV E. Finally, the pd scaling law is addressed in Sec. IV F.

A. Paschen curve and breakdown mechanisms

In Fig. 8, the Paschen curve obtained with PIC/MCC simulations is plotted and compared against the experimental data. Good agreement between these two data sets is observed in the range of applied voltage between 15 and 130 kV. The Paschen curve obtained from our numerical model is plotted up to 1 MV to show its predicted shape.

As the breakdown voltage increases, the relative roles of individual elementary physical processes accounted for in our model change along the curve. The shape of the Paschen curve can be understood by analyzing specific interactions responsible for production of ion-electron pairs. In order to do so, we also map the curve as the reduced electric field E/n versus reduced pressure pd, as shown in Fig. 8. The reduced electric field at the breakdown point varies from 75 kTd to 6600 kTd. Note that here the gas density corresponds to the temperature of 273 K. Figure 9(a) displays relative contributions by the electron, ion, and fast-atom impact ionization mechanisms to the net volume ionization rate in the gap. Figure 9(b) shows relative contributions of the positive ions, fast neutral atoms, and photons to the emission of secondary electron flux induced at the cathode. The simulations show that on the 75–950 kTd portion of the Paschen curve, with corresponding gap voltages between 15 kV and 130 kV, the contributions of electron-, ion- and fast-atom ionization are all important for sustaining the discharge. In this range, it is interesting that the share of ion-impact ionization is approximately constant at about 20%, and the share of electron-impact ionization monotonically decreases from 57% to 26%. The share of helium ionization by fast atom impact correspondingly increases from 23% to 53%. At the value $E/n = 334$ kTd, the share of fast-atom impact ionization begins to exceed that of electron-impact ionization and

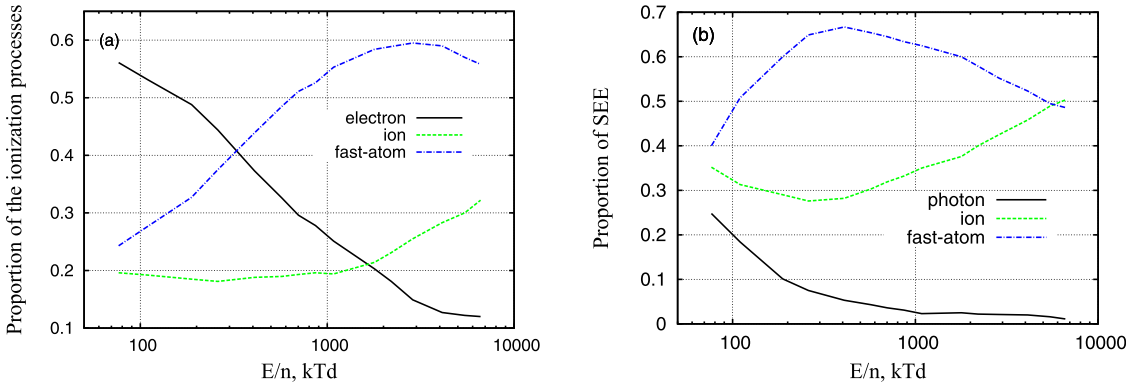

FIG. 9. (a) Fractions of ionization rate in the gap due to electron-impact ionization, ion-impact ionization, and fast-atom-impact ionization; (b) Relative contributions to inducing the secondary electron emission (SEE) flux from the cathode surface: photon impact, ion impact, and neutral atom impact.

becomes the primary ionization mechanism. In fact, in the range of 75–950 kTd, the fast atoms increasingly dominate in sustaining the discharge as the applied voltage increases, since they also yield 40%–65% of the secondary electron flux emitted from the cathode. The proportion of the ion-induced electron emission flux is about 30%, and that due to photons decreases quickly to the negligible level below 10%.

With further increase of E/n beyond 950 kTd, which is the highest value in the experimental data reported here, our PIC/MCC simulation predicts that fast neutral atoms would provide the dominant contribution to both the ionization rate and secondary electron emission. In the range of 1000 to 6600 kTd, fast-atom impact accounts for approximately 60% of the gas-phase ionization [Fig. 9(a)], and fast-atom-induced electron emission accounts for over 50% of the secondary flux. It is observed that in the vicinity of the breakdown point at 300 kV, with a corresponding reduced electric field of 2200 kTd, the Paschen curve has a turning point as seen in Fig. 8. This property is similar to the previously known turning point on the low-pressure branch of the Paschen curve for helium, observed in the "electron" regime below 1 kV in experiment[79] (with the same behavior found for mercury) as well as in numerical simulations.[13] The latter turning point exists due to transition of electrons into runaway regime[21,31] as the Townsend coefficient falls off sharply at high E/n and the multiplication length increases to become comparable with the size of the gap. The turning point observed above 100 kV, where most of the ionization is due to energetic ions and fast neutral atoms, can be understood in similar terms. What's different is that no source of "primary" ions (and hence fast neutrals) exists at the anode, and the ion velocity distribution with fully developed high-energy tail (energy is five times higher than mean ion energy) is only present at distances $\approx 5\lambda_{cx}$ and above towards the cathode.[17] For example, if $\lambda_{cx}/d = 0.1$, then only one half of the electrode gap is effectively sustaining the discharge. Therefore, $\lambda_{cx}/d = 0.1$, is a reasonable runaway criterion for energetic ions. For helium gas, the above condition (on the Paschen curve) is met at about 100 kV. The deleterious effect of increasing λ_{cx} with discharge voltage on the total ionization in the gap is counteracted by increasing the ionization cross-section of ions and (especially) more numerous fast neutrals. However, this is only true if the sufficient length ($5\lambda_{cx}$) is still available to form an energetic tail of the ion distribution. Therefore, at sufficiently high voltage, the $pd(V)$ value of the Paschen curve has to increase with voltage. In addition, the reflection yield for fast neutral atoms at the cathode falls off as an inverse power of impact energy [see Eq. (23) and Fig. 6]. Quantitatively, the role of the reflection yield for fast neutral atoms is analogous to that of the secondary ion-induced electron emission coefficient, γ, in Eq. (1), making the increase of $pd(V)$ even more pronounced. More details are provided in the follow-up paper.[80]

B. Effect of fast atom backscattering

To understand the effect of fast atom backscattering from the electrodes, we obtained Paschen curves with and without accounting for this process. The results are shown in Fig. 10. The absence of backscattered flux causes the Paschen to move to the right while keeping its shape with a turning point. At 15 kV, the breakdown value of pd is 0.59 Torr cm without artificially changing the atom reflection yield, while reducing the backscattering coefficient to zero shifts this value to 0.74 Torr cm. These observations emphasize that besides the backscattering of electrons at the anode, the backscattering of fast atoms at the cathode is essential for accurate determination of the Paschen curve.

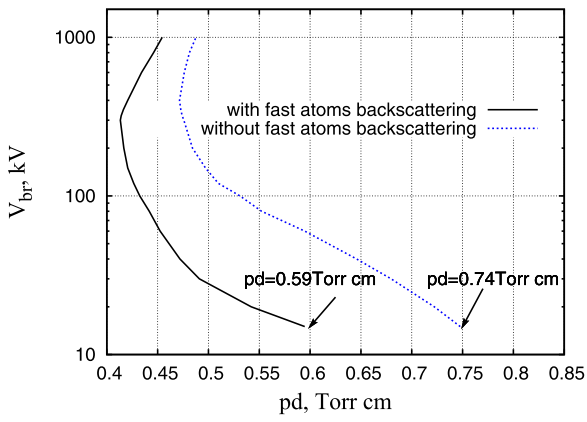

FIG. 10. Paschen curves obtained with and without fast-atom backscattering at the cathode. Disabling fast atom backscattering changes the position but not the basic shape of the Paschen curve.

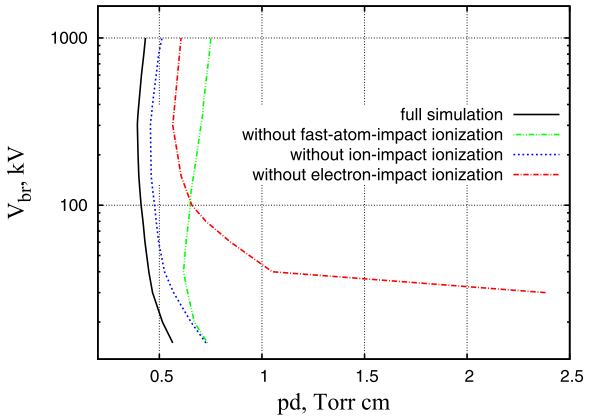

FIG. 11. Paschen curves obtained without fast-atom-impact ionization, without ion-impact ionization, and without electron-impact ionization. Electron-impact ionization dominates at low voltage but has only a small effect at high voltage, whereas fast-atom ionization must be included at high voltage to obtain the proper shape of the Paschen curve.

C. Effects of fast-neutral-, ion-, and electron-impact ionization

To investigate the relative effects of electron-, ion-, and fast-atom- impact ionization on the shape of the Paschen curve, we also carried out simulations in which one or more of these three processes were disabled. Along with the results of simulations in which all the elementary processes from Table I are fully accounted for, Fig. 11 also includes the Paschen curves obtained by neglecting:

(i) Fast-atom-impact ionization
(ii) Ion-impact ionization
(iii) Electron-impact ionization

The relative change in the breakdown value of *pd* caused by neglecting the ion-impact ionization is about 20%, which is consistent with the proportion of ion-impact ionization rate in the volume. For the simulations without fast-atom impact ionization, it is seen that above 40 kV the *pd* value will not decrease as the voltage increases. This phenomenon is attributed to the increased share of fast-atom ionization with the increase in the reduced electric field. Also, when the applied voltage is greater than 30 kV, the breakdown can still be achieved when electron-impact ionization is neglected. The resulting Paschen curve becomes closer to that found with full simulation as the voltage continues to increase. These additional observations are consistent with previous characterization of the shape of the Paschen curve in helium at high voltage. Namely, electron-impact ionization becomes less significant as the voltage increases, and the fast-atom-impact ionization rate becomes the most important factor for setting the breakdown point at very high voltage.

D. Importance of anisotropic scattering of fast atoms

In Fig. 12(a), we compare the results obtained in simulations with anisotropic and with isotropic scattering of fast neutral atoms (in the center-of-mass frame, including elastic, excitation, and ionization collisions). Note that anisotropic electron scattering is assumed in all cases as is already common practice (Sec. II C). For ions even with isotropic scattering in elastic collisions, the resonant charge-exchange collision channel always prevails, leading to ion energy distribution similar to that obtained with anisotropic scattering. Therefore, the anisotropic scattering described in Sec. II D was still applied to the ion species. The results obviously show that the isotropic-scattering simulation strongly differs from one with anisotropic scattering as well as from experimental data over the entire range of interest. The Paschen curve generated by the isotropic-scattering simulation displays a much smaller slope and the *pd* value varies from 1.21 Torr cm to 0.21 Torr cm monotonously as the voltage increases. It is found that the intersection point between the Paschen curves obtained for the isotropic-scattering case and the anisotropic-scattering case is located at about 150 kV.

The interplay between the fast atom ionization coefficient and the amount of fast atom flux helps explain why the two curves intersect. In the case of isotropic scattering of fast atoms on background thermal atoms, it is known that a fast atom loses on average about half of its energy in the lab frame, causing efficient thermalization and accumulation of "cold" neutral atoms. On the other hand, fast atom multiplication arising from the large energy transfer cross-section in the isotropic case helps sustain a high fast-atom flux. In addition, in the case of isotropic scattering, there is a large flux of fast neutrals impinging upon the electrodes at oblique angles,

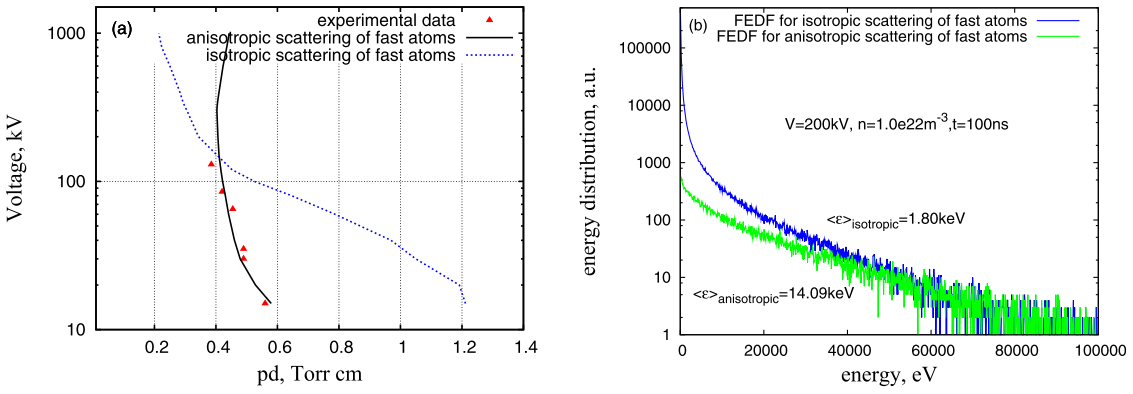

FIG. 12. Effect of anisotropic scattering of fast atoms: (a) Paschen curves obtained in anisotropic-scattering and isotropic-scattering simulations vs. the experimental data; (b) flux-energy distributions of fast neutral atoms impacting the cathode when anisotropic or isotropic scattering is assumed. The applied potential is 200 kV, the elapsed time is 100 ns, and the neutral gas density is 1.0×10^{22} m^{-3}.

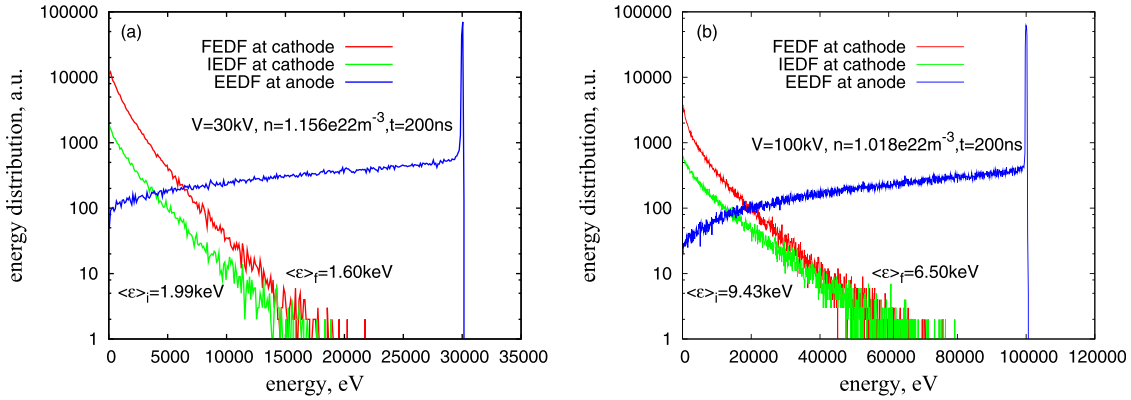

FIG. 13. IEDF (ion energy distribution function) and FEDF (fast-atom energy distribution function) at the cathode, and EEDF (electron energy distribution function) at the anode for two different breakdown voltages: (a) 30 kV, (b) 100 kV.

giving rise to larger particle and energy reflection coefficients [in accordance with Eqs. (24) and (26)]. The reflected fast atoms will induce additional ionization and also secondary electron emission.

An example is given in Fig. 12(b), showing flux-energy distributions of fast atoms at the cathode for both anisotropic and isotropic scattering in the case when the applied voltage is 200 kV and the neutral gas density is $1.0 \times 10^{22}\,\mathrm{m}^{-3}$. It is seen that the mean energies for anisotropic and isotropic scattering models are 14.09 keV and 1.80 keV, respectively (note that exact values are affected by the energy threshold for the fast neutral species imposed in our simulations). In the isotropic scattering case, the fast atoms are noticeably colder, leading to the decrease of the gas-phase ionization coefficient. However, the larger reflection coefficient and the multiplication of fast atoms due to momentum transfer in isotropic scattering will make up for the difference in the ionization rate, compared to anisotropic scattering of fast atoms, especially on the high voltage branch above 150 kV.

E. Energy distributions of the particle species

Under the conditions near the breakdown point, when the current density is small and the electric field remains uniform, it is simple to predict particle distributions at the electrodes and compare them to those observed in simulations. It should be noted that for strongly anisotropic distributions when impacts occur at near-normal incidence, energy-probability distribution of the incident flux is proportional to the velocity distribution in the volume. In other words, what is measured in experiments (or counted in simulations) is the canonical velocity distribution expressed as a function of energy, e.g., a Maxwellian would be seen as $\exp(-\varepsilon/T)$. The established experimental term is "flux-energy distribution." Throughout Sec. IV, "energy distribution" is a short for "flux-energy distribution." In Fig. 13, we show ion and fast-atom energy distributions at the cathode and the electron energy distribution at the anode under breakdown conditions at 30 kV and at 100 kV.

For electrons, the primary ones leave the cathode and are promptly accelerated to energies far exceeding the energy corresponding to the peak values of inelastic cross-sections. In fact, due to anisotropic scattering and negligible energy loss in inelastic collisions, almost all the primary electrons cross the inter-electrode gap in a "free flight" mode, leading to the pronounced peaks in the EEDFs at 30 keV and 100 keV. Likewise, the secondary electrons produced by electron-, ion-, and fast-atom-impact ionization undergo "free-fall" acceleration in the applied electric field from their initial position to acquire the energy $\varepsilon = xeV_{\mathrm{br}}/d$, where x is the initial position of a secondary electron (recalling that the anode position is at $x = 0$). These newly produced electrons form the "shoulder" portion of the EEDFs detected at the anode. In order to verify this view, we use a simple beam model with no anode backscattering to analytically connect the EEDF to the ionization source density in the 100 kV case, when the gas density at the breakdown point is $1.6 \times 10^{22}\,\mathrm{m}^{-3}$. In Fig. 14, we show the EEDF at 100 kV (except for the primary peak) calculated from the profile of the total ionization rate by converting x to ε through $\varepsilon = xeV_{\mathrm{br}}/d$. It is in excellent agreement with the electron energy distribution observed at the anode.

Next, we proceed to characterize the distributions of ions and fast atoms. When charge exchange dominates and the free path is much smaller than the electrode gap, the ion

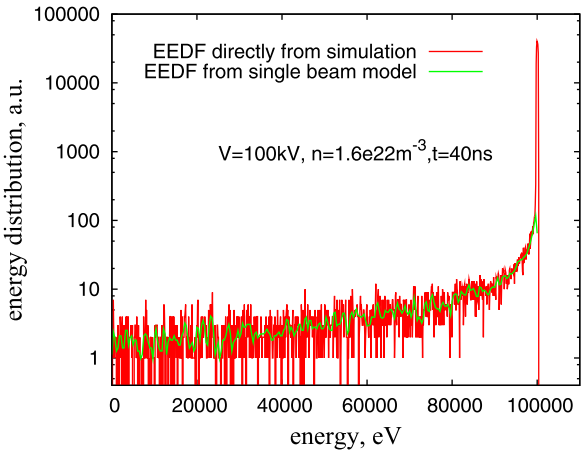

FIG. 14. Comparing the anode EEDF directly observed in simulation to that deduced from the ionization rate in a "single-beam" model. The EEDF at the anode is mostly explained by electrons that are created either at the cathode or in the gas volume, and then undergo a "free-fall" in the applied electric field towards the anode.

velocity distribution in a steady state is governed by the Boltzmann equation

$$\frac{E}{m}\frac{df}{du} = -nu\sigma_{cx}\left[\frac{mu^2}{2}\right]f, \tag{30}$$

where $\sigma_{cx}(\varepsilon) = [A - B\ln\varepsilon]^2 \times \sigma_0$ is the energy-dependent charge transfer cross-section, $\sigma_0 = 10^{-20}\text{m}^2$, the energy ε is in eV, and for helium the constants are $A = 5.282$, $B = 0.294$. The solution, up to a normalization constant determined by the flux, is

$$f(\varepsilon) = \exp\left[-\varepsilon\frac{A^2 + B^2\ln^2\varepsilon - 2(AB + B^2)(\ln\varepsilon - 1)}{E/n\sigma_0}\right]. \tag{31}$$

As noted, the energy distribution detected at the electrode is proportional to the velocity distribution in the discharge volume at the corresponding energy value. In Fig. 15, we observe a good agreement between the simulated and calculated distributions, except in the low energy range, and far in the tail where $f(\varepsilon)$ falls off by a factor of 100. The mismatch at low energies is likely due to the large number of slow ions generated by the emitted primary electrons close to the cathode, within a distance comparable to the free path for the ions.

F. The *pd* scaling of the Paschen law at extremely high *E/n*

In order to verify the validity of the *pd* scaling for the Paschen curve in the 100 kV range by means of a numerical experiment, we varied the gap size in our simulations. Note that it was not possible to vary the gap in the experimental device, and that in any experiment, it would be necessary to ensure that the field is not so strong as to cause field emission of electrons at the cathode or other phenomena leading to vacuum breakdown. The PIC/MCC simulation demonstrates that the Paschen law still holds in the 100 kV range.

For the 100 kV case as a specific example, the electrode separations of 0.7 cm, 1.4 cm, and 2.8 cm were chosen to observe and validate the *pd* scaling. The simulations show that the values of *pd* remain almost unchanged within uncertainties when the electrode separations vary between the three values. In our model, the electrons energy distribution has been demonstrated to be of a "runaway" type in the discharge gap (see Sec. IV E). However, the effective ionization cross-section $\sigma_{\text{eff}} = \alpha/n$ still shows the same dependence versus *nx* for different gap sizes with identical values of *nd*. In Fig. 16, we plot calculated effective ionization cross cross-sections of electrons, $\sigma_{\text{e,eff}}$, and of ions, $\sigma_{\text{i,eff}}$, obtained in simulations with three gap sizes of 0.7 cm, 1.4 cm, and 2.8 cm. The resulting effective ionization cross-sections for different cases, plotted against *nx*, are in excellent agreement with each other, for both electrons and ions. This means that for different gap sizes, but with the same values of *nd*, the steady-state balance shown in Fig. 3 occurs at the same voltage, and that the reduced pressure *pd* is still a valid scaling parameter.

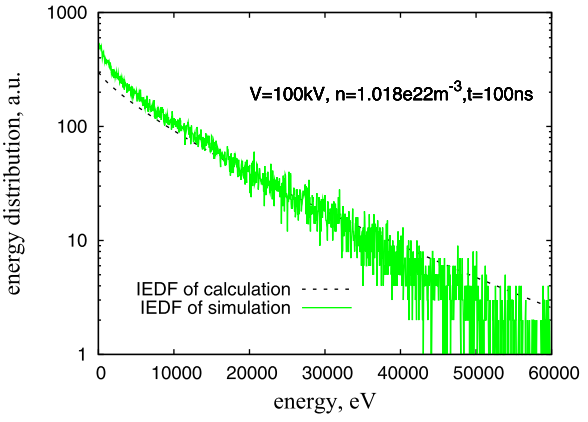

FIG. 15. Comparison of ion energy distributions for the 100 kV breakdown case from the simulation and from the calculation.

V. CONCLUSION

The breakdown properties of helium for the applied voltage in the range of 100–1000 kV at $pd < 1$ Torr cm have been investigated experimentally and by means of the PIC/MCC simulation technique. In our model, energy-dependent anisotropic scattering for electrons, ions, and fast atoms has been implemented to adequately describe particle collisions in the gas phase. The backscattering of fast heavy particles (neutral atoms and ions) at both electrodes is also taken into account, as well as electron backscattering at the anode. The Paschen curve obtained in our simulations agrees quite well with the experimental data obtained in the range of 15–130 kV.

Sensitivity studies of the Paschen curve have been performed with respect to the primary input parameters of the physical model. We find large differences between the Paschen curves obtained with anisotropic and with isotropic scattering for ions and fast atoms, demonstrating that anisotropic scattering for each of the three species on the background gas is essential for reproducing the physics of the breakdown process. Test results further indicate that the following two processes are important for setting the breakdown condition in the 100 kV regime for helium, in addition

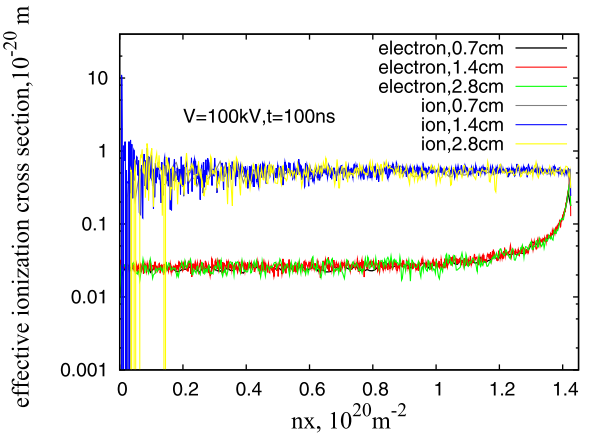

FIG. 16. Simulation results showing effective ionization cross-section of electrons $\sigma_{\text{e,eff}}$ and of ions $\sigma_{\text{i,eff}}$ for three gap sizes of 0.7 cm, 1.4 cm, and 2.8 cm, plotted versus the scaled distance *nx*. The product of pressure and distance is a valid scaling variable for the Paschen curve at both low and high voltages.

to the electron- and ion-impact ionization, and ion- and fast-atom-induced secondary electron yield:

(i) Fast-atom backscattering at the cathode
(ii) Fast-atom-impact ionization.

In summary, fast atoms increasingly affect the ionization balance as the applied voltage increases, due to

(i) Increasing ionization cross-section vs. energy.
(ii) The copious flux of energetic fast atoms generated in charge-exchange collisions.
(iii) Typically in the regime of interest, over a half of the electron flux emitted from the cathode being induced by fast neutral atoms.
(iv) The flux of fast atoms backscattered from the cathode helping sustain the ionization.

ACKNOWLEDGMENTS

The authors are indebted to Dr. Dmytro Sydorenko, the developer of the EDIPIC code. The work of L. Xu was supported by the Chinese Scholarship Council and of other authors by the Advanced Research Projects Agency-Energy (ARPA-E), U.S. Department of Energy, under Award No. DE-AR0000298.

[1]J. S. Townsend, *Electricity in Gases* (Clarendon Press, Oxford, 1915).
[2]M. J. Druyvesteyn and F. M. Penning, Rev. Mod. Phys. **12**, 87 (1940).
[3]J. M. Meeks and J. D. Craggs, *Electrical Breakdown of Gases* (Clarendon Press, Oxford, 1953).
[4]M. J. Schönhuber, IEEE Trans. Power Appar. Syst. **PAS-88**, 100 (1969).
[5]J. D. Pace and A. B. Parker, J. Phys. D: Appl. Phys. **6**, 1525 (1973).
[6]A. H. Cookson, IEE Proc. A **128**, 303 (1981).
[7]A. V. Phelps and Z. L. Petrovic, Plasma Sources Sci. Technol. **8**, R21–R44 (1999).
[8]M. Radmilović-Radjenović, Z. Petrović, G. Malović, D. Marić, and B. Radjenović, Czech. J. Phys. **56**(2), B996 (2006).
[9]P. Osmokrovic, T. Zivic, B. Loncar, and A. Vasic, Plasma Sources Sci. Technol. **15**, 703 (2006).
[10]V. A. Lisovskiy, S. D. Yakovin, and V. D. Yegorenkov, J. Phys. D: Appl. Phys. **33**, 2722 (2000).
[11]V. A. Lisovskiy, V. A. Koval, and V. D. Yegorenkov, Phys. Lett. A **375**, 1986 (2011).
[12]B. M. Jelenković and A. V. Phelps, Phys. Rev. E **71**, 016410 (2005).
[13]P. Hartmann, Z. Donko, G. Bano, L. Szalai, and K. Rozsa, Plasma Sources Sci. Technol. **9**, 183 (2000).
[14]G. W. McClure and K. D. Granzow, Phys. Rev. **125**, 3 (1962).
[15]K. D. Granzow and G. W. McClure, Phys. Rev. **125**, 1792 (1962).
[16]D. Bhasavanich and A. Parker, Proc. R. Soc. A **358**, 385 (1978).
[17]E. J. Lauer, S. S. Yu, and D. M. Cox, Phys. Rev. A **23**, 2250 (1981).
[18]M. A. Lieberman and A. J. Lichtenberg, *Principles of Plasma Discharges and Materials Processing* (Wiley, New York, 1994).
[19]F. M. Penning, Proc. R. Soc. Amsterdam **34**, 1305 (1931).
[20]J. Fletcher, J. Phys. D: Appl. Phys. **18**, 221 (1985).
[21]L. D. Tsendin, Tech. Phys. Lett. **35**, 1044 (2009).
[22]A. N. Dikidzhi and B. N. Klyarfel'd, Zh. Tekh. Fiz. **25**, 1038 (1955).
[23]H. Hillmann, F. Muller, and H. Wenz, Plasma Sources Sci. Technol. **3**, 496 (1994).
[24]Z. Donkó, Phys. Rev. E **64**, 26401 (2001).
[25]A. V. Phelps and B. M. Jelenković, Phys. Rev. A **38**, 2975 (1988).
[26]M. V. V. S. Rao, R. J. Van Brunt, and J. K. Olthoff, Phys. Rev. E **54**, 5641 (1996).
[27]J. E. Lawler, Phys. Rev. A **32**, 2977 (1985).
[28]D. Sydorenko, "Particle-in-cell simulations of electron dynamics in low pressure discharges with magnetic fields," Ph.D. thesis (University of Saskatchewan, Sascatoon, 2006).
[29]D. Sydorenko, I. Kaganovich, Y. Raitses, and A. Smolyakov, Phys. Rev. Lett. **103**, 145004 (2009).
[30]J. Carlsson, A. Khrabrov, I. Kaganovich, T. Sommerer, and D. Keating, Plasma Sources Sci. Technol. **26**, 014003 (2017).
[31]A. N. Tkachev and S. I. Yakovlenko, JETP Lett. **77**, 221 (2003).
[32]L. Alves, K. Bartschat, S. Biagi, M. Bordage, L. Pitchford, C. Ferreira, G. Hagelaar, W. Morgan, S. Pancheshnyi, A. Phelps *et al.*, J. Phys. D: Appl. Phys. **46**, 334002 (2013).
[33]Y. Ralchenko, R. Janev, T. Kato, D. Fursa, I. Bray, and F. de Heer, At. Data Nucl. Data Tables **94**, 603 (2008).
[34]W. H. Cramer and J. H. Simons, J. Chem. Phys. **26**(5), 1272 (1957).
[35]R. Hegerberg, T. Stefansson, and M. T. Elford, J. Phys. B: At. Mol. Phys. **11**, 133 (1978).
[36]R. Okasaka, Y. Konishi, Y. Sato, and K. Fukuda, J. Phys. B: At. Mol. Phys. **20**, 3771 (1987).
[37]H. B. Gilbody and J. B. Hasted, Proc. R. Soc. A **240**(1122), 382 (1957).
[38]A. V. Phelps, see https://jila.colorado.edu/~avp/collision_data/ for cross-section data on elastic scattering of neutral helium atoms on each other.
[39]V. Kempter, F. Veith, and L. Zehnle, J. Phys. B: At. Mol. Phys. **8**(7), 1041 (1975).
[40]H. C. Hayden and N. G. Utterback, Phys. Rev. **135**(6A), A1575 (1964).
[41]C. F. Barnett, "Atomic data for fusion, v. 1," Oak Ridge National Laboratory Report ORNL-6086/V1, 1990.
[42]P. Rudnick, Phys. Rev. **38**, 1342 (1931).
[43]A. Rostagni, Nuovo Cimento **11**, 621 (1934).
[44]R. H. Hammond, J. M. S. Henis, and E. F. GreeneJohn Ross, J. Chem. Phys. **55**, 3506 (1971).
[45]N. Noda, J. Phys. Soc. Jpn. **41**, 625 (1976).
[46]P. Rosen, Phys. Rev. **109**, 348 (1958).
[47]J. A. Kunc and W. H. Soon, J. Chem. Phys. **95**, 5738 (1991).
[48]H. B. Gilbody, K. F. Dunn, R. Browning, and C. J. Latimer, J. Phys. B: At. Mol. Phys. **4**, 800 (1971).
[49]D. P. Sural, S. C. Mukherjee, and N. C. Sil, Phys. Rev. **164**, 156 (1967).
[50]P. J. MacVicar-Whelan and W. L. Borst, Phys. Rev. A **1**, 314 (1970).
[51]K. B. Fiering, S. R. Ryan, and W. H. Wing, J. Phys. B: At. Mol. Phys. **15**, 3841 (1982).
[52]M. Hollstein, J. R. Sheridan, J. R. Peterson, and D. C. Lorents, Phys. Rev. **187**, 118 (1969).
[53]E. Horsdall Pedersen, J. Heinemeier, L. Larsen, and J. V. Miikkelsen, J. Phys. B: At. Mol. Phys. **13**, 1167 (1980).
[54]M. E. Rudd, T. V. Goffe, A. Itoh, and R. D. DuBois, Phys. Rev. A **32**, 829 (1985).
[55]R. D. DuBois, Phys. Rev. A **39**, 4440 (1989).
[56]V. P. Shevelko, D. Kato, M.-Y. Song, H. Tawara, I. Y. Tolstikhina, and J.-S. Yoon, "One-electron capture and target ionization in He+-neutral-atom collisions," National Institute for Fusion Science Report NIFS-DATA-107, Toki, Japan, 2009.
[57]H. Tawara, J. Phys. Soc. Jpn. **31**, 236 (1971).
[58]E. S. Solov'ev, R. N. Il'in, V. Oparin, and N. V. Fedorenko, Sov. Phys. - JETP **18**, 342 (1964).
[59]Y. M. Fogel', V. A. Ankudinov, and D. V. Pilipenko, Sov. Phys. - JETP **11**, 18 (1960).
[60]C. Barnett and P. Stier, Phys. Rev. **109**, 385 (1958).
[61]P. Pradel, P. Monchicourt, D. Dubreuil, and J. J. Laucagne, Phys. Rev. A **35**, 1062 (1987).
[62]Y. A. Kudryavtsev and V. V. Petrunin, Sov. Phys. JETP **72**, 43 (1991).
[63]S. K. Allison, Rev. Mod. Phys. **30**, 1137 (1958).
[64]N. V. Novikov and Y. A. Teplova, see http://cdfe.sinp.msu.ru/services/cccs/HTM/main.htm for Charge-Changing Cross Sections in Ion-Atom Collisions, Institute of Nuclear Physics, Moscow State University, Moscow, Russia.
[65]A. Okhrimovskyy, A. Bogaerts, and R. Gijbels, Phys. Rev. E **65**, 37402 (2002).
[66]G. Wentzel, Z. Phys. **40**, 590 (1926).
[67]A. V. Khrabrov and I. D. Kaganovich, Phys. Plasmas **19**, 93511 (2012).
[68]C. B. Opal, W. K. Peterson, and E. C. Beaty, J. Chem. Phys **55**(8), 4100 (1971).
[69]S. Yoshida, A. Phelps, and L. Pitchford, Phys. Rev. A **27**, 2858 (1983).
[70]H. Wang, V. S. Sukhomlinov, I. D. Kaganovich, and A. S. Mustafaev, Plasma Sources Sci. Technol. **26**, 24001 (2017).
[71]P. A. Bokhan and D. E. Zakrevsky, Tech. Phys. **52**, 104 (2007).
[72]B. Szapiro, J. J. Rocca, and T. Prabhuram, Appl. Phys. Lett. **53**(5), 358 (1988).
[73]L. Marton and C. Marton, *Advances in Electronics and Electron Physics* (Academic Press, New York, London, 1980), Vol. 50.

[74]K. H. Krebs, Fortschr. Phys. **16**, 419 (1968).
[75]E. H. Darlington, J. Phys. D: Appl. Phys. **8**, 85 (1975).
[76]K. S. Min, B. J. Park, J. B. Park, S. K. Kang, and G. Y. Yeom, J. Korean Phys. Soc. **51**, 967 (2007).
[77]W. Eckstein, Bull. Russ. Acad. Sci.: Phys. **74**, 141 (2010).
[78]D. M. Goebel, Rev. Sci. Instrum. **67**(9), 3136 (1996).
[79]L. G. Guseva, "On discharge striking in polyatomic gases at pd $<$ (pd)min," in *Investigations into Electrical Discharges in Gases*, edited by B. N. Klyarfel'd (Elsevier, New York, 1964), pp. 1–11.
[80]L. Xu, A. V. Khrabrov, I. D. Kaganovich, and T. J. Sommerer, "Analysis of cold-cathode breakdown in helium at extremely high electric field and low pressure," Phys. Plasmas (unpublished).